



Direct Synthesis of Dimethyl Carbonate from Methanol and Carbon Dioxide Catalyzed by Cerium-Based High-Entropy Oxides

Yunhan Gu¹ · Qingyan Cheng^{1,2} · Xu Li¹ · Shuai Zhang¹ · Zhuo Wang¹ · Yanji Wang^{1,2}

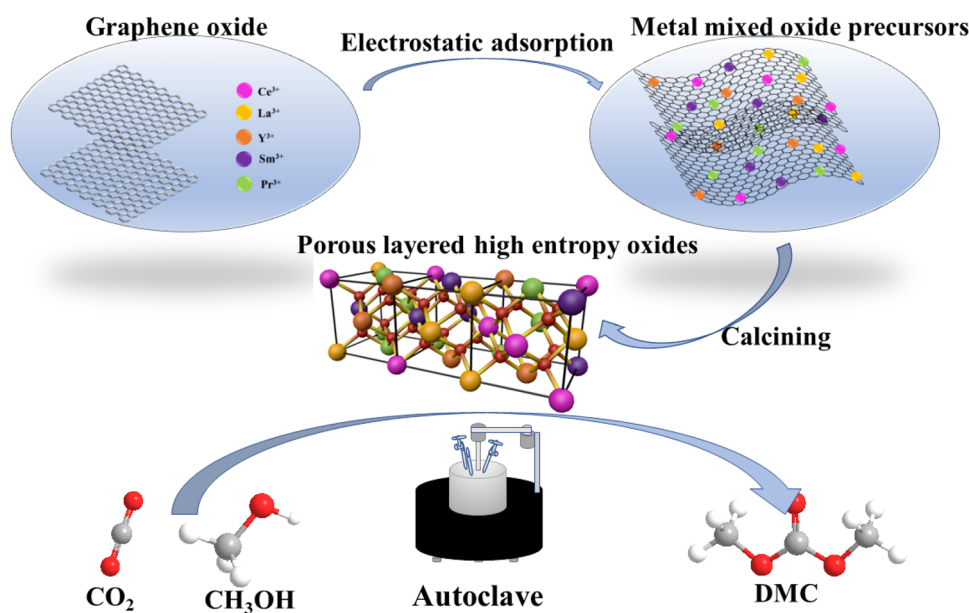
Received: 22 November 2022 / Accepted: 10 February 2023 / Published online: 3 March 2023
© The Author(s), under exclusive licence to Springer Science+Business Media, LLC, part of Springer Nature 2023

Abstract

Fluorite high entropy oxides (HEOs) were synthesized by anchoring method and $\text{Ce}_{0.5}(\text{LaPrSmY})_{0.5}\text{O}_{2-y}$ used as catalysts for synthesis of dimethyl carbonate (DMC) from methanol (CH_3OH) and carbon dioxide (CO_2), the yield of DMC was up to 7.6 mmol/g at 140 °C and 8.0 MPa. Under the same reaction conditions, the time to reach reaction equilibrium was reduced by half compared HEOs with CeO_2 . The structure of HEOs were characterized by X-ray diffraction (XRD), specific surface area and pore size analyzer (BET), high-resolution transmission electron microscopy (HRTEM) and X-ray photoelectron spectroscopy (XPS). The results showed that there are five metal elements of Ce, La, Pr, Sm and Y in the lattice of layered fluorite-type HEOs $\text{Ce}_x(\text{LaPrSmY})_{1-x}\text{O}_{2-y}$. The synergistic effect among the elements led to the lattice distortion and the generation of a large number of oxygen vacancies, which improved the reaction rate.

Graphical Abstract

The rare earth metal ions were anchored on the graphene oxide by electrostatic interaction and then calcinated to obtain fluorite high entropy oxides (HEOs) $\text{Ce}_x(\text{LaPrSmY})_{1-x}\text{O}_{2-y}$. $\text{Ce}_{0.5}(\text{LaPrSmY})_{0.5}\text{O}_{2-y}$ were used as catalysts for synthesis of dimethyl carbonate (DMC) from methanol (CH_3OH) and carbon dioxide (CO_2), the yield of DMC was up to 7.6 mmol/g at 140 °C and 8.0 MPa. Under the same reaction conditions, the time to reach reaction equilibrium was reduced by half compared with CeO_2 attributed to the abundant oxygen vacancies on the surface and the excellent electron transfer ability.



Keywords High entropy oxide · Catalyst · Dimethyl carbonate · Anchoring method · Oxygen vacancy

Extended author information available on the last page of the article

1 Introduction

HEOs are single phase solid solutions consisting of five or more elements [1, 2]. The first appearance of HEOs in the literature was in 2015 [3], it has received increasing attention due to its high stability, low thermal conductivity, high corrosion resistance, oxidation resistance, and high catalytic activity [4, 5]. HEOs prepared by non-traditional synthesis methods (arc melting and spark plasma sintering) possessed an entropy stable system with a specific composition and structure [6, 7], but the catalytic performance of HEOs were limited, by only part of active sites in HEOs being exposed to the surface of the material due to high temperature. The cations in HEOs are composed of same or similar proportions incorporated into the cationic sub-lattice, and the average radius of cations is one of the most important factors affecting the crystal of HEOs [7–9].

Since 2000, rare earth oxide materials have received widespread attention in various research areas such as photocatalysis, energy storage and conversion, and electrochemistry, and a series of far-reaching research results have been achieved [10–12]. Rare-earth elements exhibit highly similar ionic radii and physicochemical properties [13]. Most of the high entropy compositions that were successfully prepared as single phases are within the 15% limit of atomic radii differences known as a Hume-Rothery [14] rule to metallurgists and as a Goldschmidt [15] limit for isomorphous mixtures to mineralogists. The combination of several (five or more) rare earth elements with highly similar ionic radii and physicochemical properties into a specific structure allows better formation of high entropy oxides with a single crystalline phase [16].

DMC as a ‘green solvent’ in the chemical industry, is an important chemical intermediate with a wide range of applications in many fields [17–19]. The demand for DMC is increasing year by year due to its wide range of application scenarios. Traditional synthetic routes suffered from various drawbacks [19–24]. The direct synthesis of DMC from CH_3OH and CO_2 has the advantages of abundant raw materials, environmental friendliness and high atomic economy. However, the direct synthesis method was limited by kinetic and thermodynamic factors, and the conversion of CH_3OH

as well as the reaction rate was low [25–27]. The Ce catalyst possessed excellent catalytic performance in the direct synthesis of DMC from CO_2 and CH_3OH [28–30].

In this paper, rare earth element fluorite HEO was synthesized by anchoring method, and its catalytic performance in the direct synthesis of DMC from CO_2 and CH_3OH was investigated. During the formation process of HEOs, rare earth metal cations were adsorbed by the negative functional groups on the surface of graphene oxide, which could prevent effectively the agglomeration of precursor nanoparticles during heating [31]. Then, a porous single-phase fluorite-type HEOs are formed by high-temperature calcination.

1.1 Materials

$\text{Ce}(\text{NO}_3)_3 \cdot 6\text{H}_2\text{O}$, $\text{La}(\text{NO}_3)_3 \cdot n\text{H}_2\text{O}$, $\text{Sm}(\text{NO}_3)_3 \cdot 6\text{H}_2\text{O}$, $\text{Pr}(\text{NO}_3)_3 \cdot 6\text{H}_2\text{O}$, $\text{Y}(\text{NO}_3)_3 \cdot 6\text{H}_2\text{O}$, CH_3OH , n-Butanol ($\text{CH}_3(\text{CH}_2)_3\text{OH}$), Ethylene glycol ($(\text{CH}_2\text{OH})_2$), Dimethyl carbonate ($\text{C}_3\text{H}_6\text{O}_3$), were from, Ron company (Shang hai, China). All reagents were of analytical grade and were used as received. CO_2 (99.99%), N_2 (> 99.99%).

1.2 Preparation of Catalyst

The formation diagram of porous layered HEOs were shown in Fig. 1. The typical synthesis process was shown in Fig. 2: 100 mg of graphene oxide was dissolved in 50 mL of ethylene glycol, a certain molar ratio of Sm, La, Ce, Pr and Y

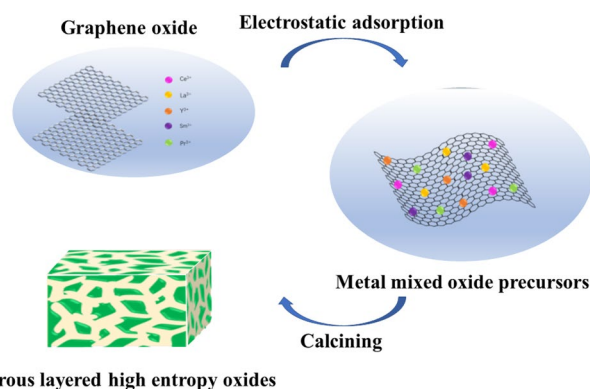
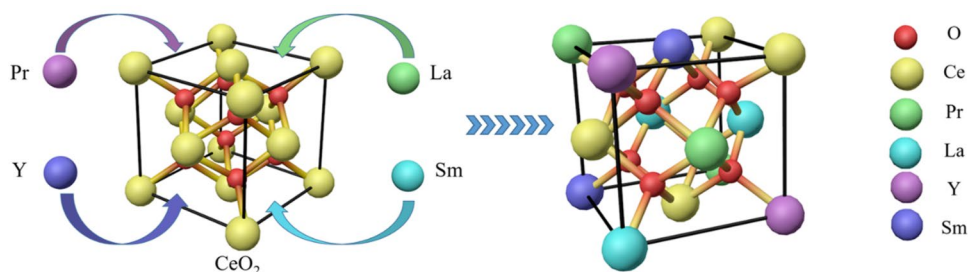


Fig. 2 Schematic illustration of the formation process for holey HEOs

Fig. 1 The formation concept of HEOs



nitrate were dissolved in 30 mL of ethylene glycol, and each of them was sonicated for 30 min. Then the two solutions were mixed and continued to be ultrasonically dispersed for 60 min to make the solution mixed uniformly. The the solution was poured into flasks and refluxed for 4 h in 170 °C oil bath. The product was separated by centrifugation, washed and precipitated three times with anhydrous ethanol, and then dried in a vacuum oven at 60 °C for 6 h. The obtained precursors were calcined at 500 °C, 750 °C and 1000 °C for 2 h in air to obtain porous layered HEOs $Ce_x(LaPrSmY)_{1-x}O_{2-y}$ ('x', the molar ratio of Ce ions in the metal cation of HEOs; '1-x', the molar ratio of metal cation M (M=La, Pr, Sm and Y) in the metal cation of HEOs; '2-y', the molar amount of oxygen atoms of HEOs to maintain electrical neutrality.). Prepared $Ce_{0.2}(LaPrSmY)_{0.8}O_{2-y}$ were named HEO-500, HEO-750 and HEO-1000.

1.3 Catalyst Evaluation

The catalyst performance test was carried out in an autoclave. A certain amount of catalyst and 15 mL CH_3OH were put into a high-pressure reactor with PTFE lining. The reactor was installed according to the operation and the gas tightness of the device was good during the reaction, and then CO_2 was introduced three times to replace the air in the autoclave. Finally, the reactor was filled with 4 MPa CO_2 (initial pressure). The temperature was set to rise from room temperature to 140 °C in 30 min and kept at 140 °C for a certain time. After reaction, the product was analyzed by gas chromatography (Agilent 7890B). The yield of DMC was quantified using the internal standard method, with n-butanol as the internal standard, and the calculation procedure is as follows [32].

$$W_{DMC} = f_{DMC} \frac{A_{DMC}}{\frac{A_s}{W_s}} \quad (1)$$

$$n_{DMC} = \frac{W_{DMC}}{M_{DMC}} \quad (2)$$

$$Y_{DMC} = \left(\frac{n_{DMC}}{m_{catalyst}} \right) \quad (3)$$

f_{DMC} : Relative mass correction factor of DMC. A_{DMC} : Peak area of DMC. A_s : Peak area of n-butanol. W_s : Mass of internal standard n-butanol in the sample. W_{DMC} : Mass of DMC in the sample. M_{DMC} : Molar mass of DMC. n_{DMC} : Amount of substance of DMC. $m_{catalyst}$: Quality of catalyst. Y_{DMC} : The yield of DMC

1.4 Characterization

An X-ray diffractometer manufactured by German Brook AXS Company was used to test and analyze the crystal structures of samples (wide-angle scanning range: 20°–90°; scanning speed: 6°/min). Nitrogen adsorption–desorption measurements were performed at 90 °C using an ASAP 2020 analyzer utilizing the BET model for the calculation of specific surface areas. Micromeritics Auto Chem 2920 automatic programmed temperature chemical adsorption instrument, test conditions: 90 °C, vacuum degassing 8 h, adsorbate N_2 , carrier gas He. The catalyst particles were observed using Talos F200S field emission high-resolution transmission electron microscope with the pressurization voltage set to 200 kV. The analysis of surface elements was performed on X-ray photoelectron spectroscopy (XPS), Thermo Fisher Scientific Escalab 250Xi spectrometer with Al Kalpha radiation as the excitation source.

2 Results and Discussion

2.1 Catalyst Characterization

2.1.1 XRD

XRD patterns of CeO_2 and a series of HEOs prepared at different calcination temperature were shown in Fig. 3. There was no obvious characteristic peak observed when HEOs being calcined at 500 °C, indicating that the sample was not strongly crystalline. When the calcination temperature was increased to 750 °C, a series of multi-phase mixture peaks appeared in the XRD pattern. At this time, the graphene oxide had not been completely removed from the surface of the HEOs crystals. Moreover, the characteristic absorption peak intensity of HEOs in the figure was weakened and the half-peak width was widen, indicating that the sample was weakly crystalline and the nanoparticles were not completely dispersed. When the calcination temperature was increased to 1000 °C, the HEOs exhibited the same characteristic peaks as CeO_2 , which could indicate HEOs were transformed from a multiphase mixture to a face-centered cubic structure with a single crystalline phase, and the graphene oxide was completely removed. In addition, the XRD pattern of HEO-1000 illustrates that all the rare earth metal elements entered the fluorite crystalline phase with small half-peak widths of characteristic peaks and good crystallinity [33, 34]. This is in agreement with the previous report of Hao Chen et al., that the key to the formation of high entropy oxides is being treated at high temperature [4]. From the XRD pattern and the calculation of Scherrer's formula in Jade, it could be concluded that the sample lattice parameter is 5.35 Å, which was smaller than the lattice parameter of CeO_2 (5.411 Å),

Fig. 3 XRD patterns of CeO_2 and holey HEOs prepared at different calcination temperature: (a) CeO_2 , (b) HEO-1000, (c) HEO-750, (d) HEO-500

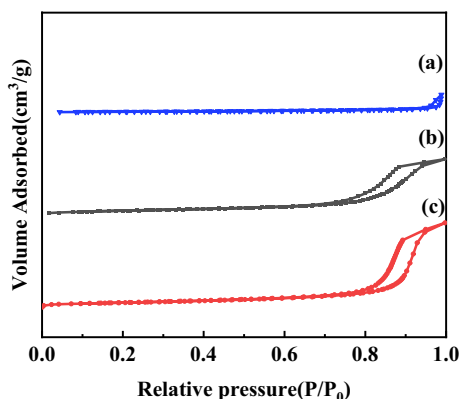
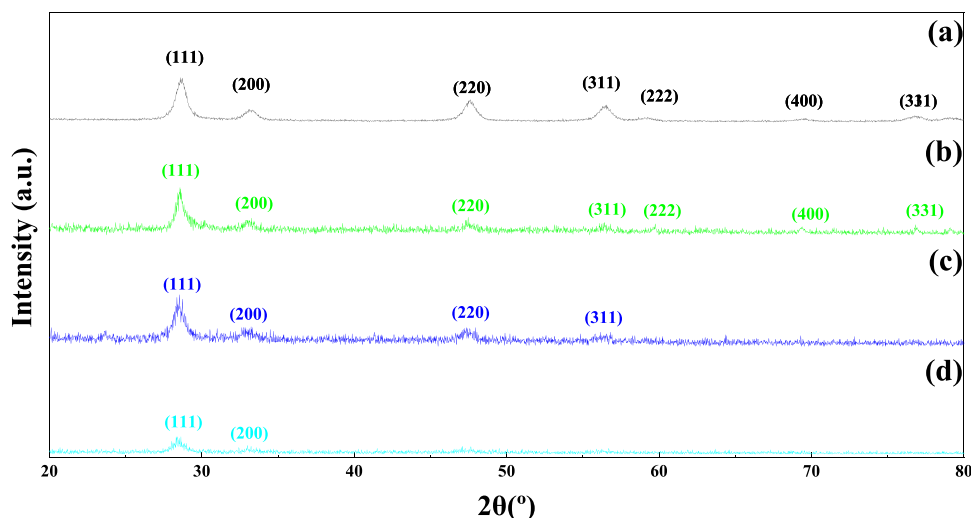


Fig. 4 N_2 adsorption–desorption isotherms of holey HEOs prepared at different calcination temperature: (a) HEO-500, (b) HEO-750, (c) HEO-1000

probably due to the fact that the radii of all other ions are slightly smaller than Ce^{4+} .

2.1.2 BET

The N_2 adsorption–desorption test of HEOs catalysts prepared at different calcination temperature was carried out, and the results were shown in Fig. 4. It could be seen from the adsorption isotherms of HEOs calcined at 500 °C that there was no saturated adsorption platform and hysteresis loop. It showed that the pore structure of the catalyst was very irregular, only a few of the catalyst particles were accumulated into slit pores, which was still in the multiphase amorphous state, and the specific surface area of the solid solution was only $37 \text{ m}^2 \cdot \text{g}^{-1}$. The adsorption isotherms of HEOs calcined at 750 °C and 1000 °C showed IV type characteristics at $P/P_0 = 0.6$, indicating that the catalysts formed a mesoporous structure and an H2 type hysteresis loop [35].

The hysteresis loop of HEOs calcined at 1000 °C appears later than that of HEOs calcined at 750 °C. When the pressure was enough to cause capillary condensation, the larger the pore size on the surface of the solid solution, the higher the pressure at which capillary condensation occurred, indicating that the pore size of the solid solution calcined at 1000 °C is bigger [36, 37]. However, the layered structure of HEOs calcined at 1000 °C was more regular, and the specific surface area of solid solution was $100 \text{ m}^2 \cdot \text{g}^{-1}$, while the specific surface area of HEOs calcined at 750 °C was $64 \text{ m}^2 \cdot \text{g}^{-1}$.

2.1.3 TEM and EDS

The TEM images of porous layered HEOs calcined at 1000 °C, 750 °C and 500 °C were shown in Fig. 5(a)–(c), respectively. When the calcination temperature of 500 °C and 750 °C, it could be clearly observed that the HEOs particles were not completely dispersed. The black shadows in Fig. 5(b) and 5(c) showed that some atoms of HEOs were still in the state of aggregation at this time, and there were some collapses and graphite residues between layers. The uniformly dispersed nanoparticles were formed after HEOs were calcined at 1000 °C, and the particles were interconnected to form the pore walls of porous structure, which was consistent with the results of XRD analysis. Attributed to ethylene glycol as a surfactant in the preparation of the precursor, not only the size of the nanoparticles could be well controlled, but also the spontaneous agglomeration of the synthesized nanoparticles could be reduced, ensuring the high dispersion of metal ions [38, 39]. The average particle size of HEO-1000 particles was about 15–25 nm.

The microstructure of HEO-1000 at the atomic scale was visualized by HRTEM, and the image was shown in Fig. 5(d). HEO-1000 showed only one type of lattice stripe, indicating that HEO-1000 is a single-crystal structure with a lattice spacing of 0.241 nm, corresponding to the (111)

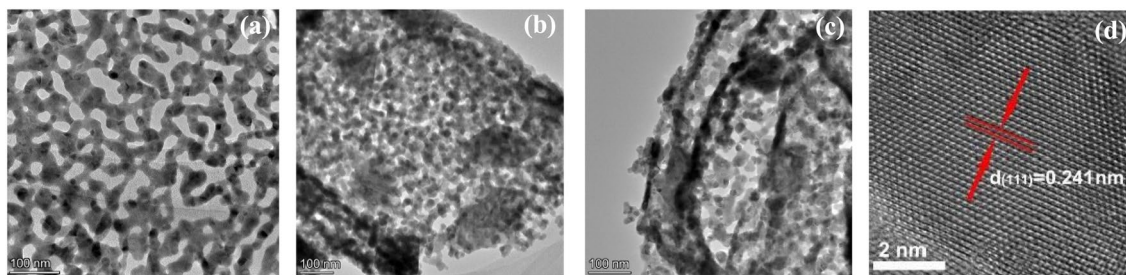


Fig. 5 TEM images of holey HEOs at different calcination temperature: (a) 1000 °C, (b) 750 °C, (c) 500 °C, (d) HRTEM images

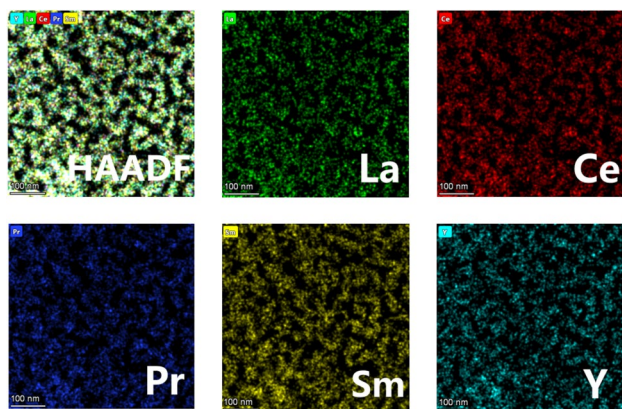


Fig. 6 Elemental mapping images of HEO-1000

lattice with the highest intensity of diffraction peaks in the high-entropy oxide [40]. Combined with the XRD patterns, it was concluded that high-temperature calcination was necessary for the formation of a single fluorite type HEOs.

Elemental dispersion played an important role for the formation of high entropy structures in HEOs, the element mapping diagram of HEO-1000 were shown in Fig. 6. The distribution of Ce, La, Pr, Sm and Y in the material could be seen in the Fig. 6, and no local aggregation of one or several elements was found on the microscopic scale. It shown that the elements in the sample were uniformly distributed and formed a single-phase high entropy structure. Meanwhile, it could be speculated that the uniform distribution of Ce, La, Pr, Sm and Y in the fluorite unit cell is consistent to the highest configuration entropy model theory. That is, the stability of the whole system is the strongest when the configuration entropy of HEOs is the biggest [41, 42].

2.1.4 XPS

The surface valence of the elements in the HEO-1000 catalyst were determined by XPS, and the results were shown in Fig. 7. The O 1 s peaks can be well fitted with three peaks due to the lattice oxygen located at 528.5 eV, oxygen vacancies located at 531.0 eV and surface oxygen located

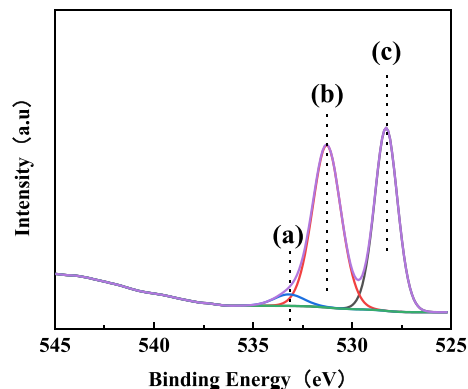


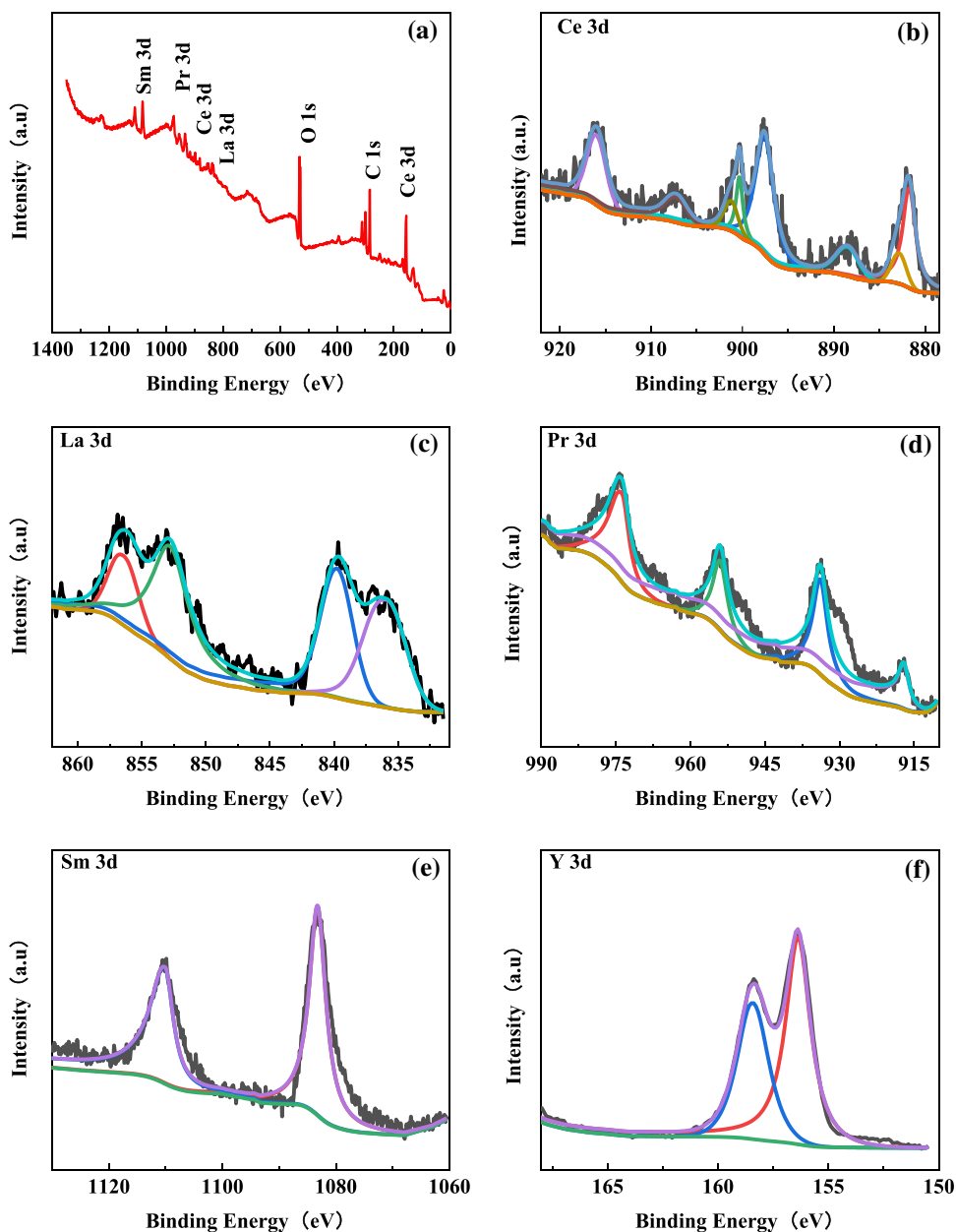
Fig. 7 O 1s XPS spectra of HEO-1000 sample: (a) O_C , (b) O_V , (c) O_L

at 533 eV [43]. The intensity of the oxygen vacancy peak represents the content of oxygen vacancies on the catalyst surface, indicating the strength of the redox ability of the catalyst [44, 45]. By XPS quantitative analysis of these three types of oxygen, it was found that the oxygen vacancy content in porous layered HEOs were as high as 29%, while higher oxygen vacancy content increased the ability of the catalyst to adsorb CO_2 and activate CH_3OH . The formula is as follows:

$$C[O_V\%] = \left(\frac{AO_V}{AO_L + AO_C + AO_V} \right) \times 100\% \quad (4)$$

Figure 8 was the XPS spectra of HEO-1000, including Ce, La, Pr, Sm and Y, indicating the formation of a good five-element solid solution structure, which was consistent with the element mapping results in Fig. 6. In the XPS spectra of the metal elements, the Ce 3d spectra could be fitted to eight peaks, four V peaks and four U peaks, namely, V (~882.4 eV), V' (~883.2 eV), V'' (~888.7 eV), V''' (~898.1 eV), U (~900.9 eV), U' (~902.8 eV), U'' (~907.4 eV) and U''' (~916.4 eV). where V, V'', V''' and U, U'', U''' denoted the electronic states of Ce^{4+} and V' and U' denoted the electronic states of Ce^{3+} [30]. La 3d_{3/2} and La 3d_{5/2} at 853.1 and 835.7 eV characteristic peaks attributed to La^{3+} [46]. The characteristic peaks located at 933.8 eV and

Fig. 8 XPS spectra of HEO-1000 sample: (a) Broad spectrum, (b) Ce 3d, (c) La 3d, (d) Pr 3d, (e) Sm 3d, (f) Y 3d



954.3 eV should be attributed to Pr 3d_{2/5} and Pr 3d_{2/3} of Pr³⁺ in HEO-1000. The other two surrounding satellite peaks might be due to the presence of unpaired electrons in the Pr hybrid orbitals and spin states [47]. The characteristic peaks located at about 1083.3 eV and 110.4 eV were attributed to Sm 3d_{5/2} and Sm 3d_{3/2} of Sm³⁺ [47], the characteristic peaks located at 156.5 eV and 158.8 eV were attributed to Y 3d_{5/2} and Y 3d_{3/2} of Y³⁺ [46]. In addition, XPS spectra showed that the binding energy of each element in HEO-1000 was strong compared to that of oxides composed of a single rare earth element [48–52]. The shift of elemental bond energy to higher positions indicated not only the formation of alloy-like species, but also a higher positive charge of all metal

elements, which made it easier for the reactants to react on HEO-1000 and improved the catalytic performance.

2.1.5 H₂-TPR

H₂-TPR experiments were performed in order to evaluate the redox ability of HEO-1000 and the results were shown in Fig. 9. The reduction peak at 462.4 °C was attributed to the removal of lattice oxygen from the surface and subsurface. The reduction peak at 757.5 °C could be interpreted as the elimination of lattice oxygen in HEO-1000. The reduction peak at 287.9 °C was attributed to the removal of adsorbed oxygen from the surface, which could indicate that HEO-1000 possesses abundant oxygen vacancies and therefore

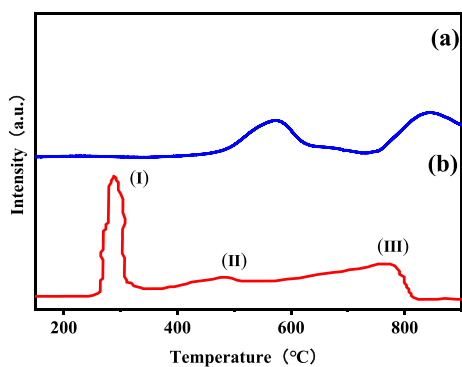


Fig. 9 H₂-TPR profiles of samples: (a) CeO₂, (b) HEO-1000. (I) 287.9 °C, (II) 462.4 °C, (III) 757.5 °C

could capture a large amount of adsorbed oxygen [45, 53]. The three peaks appearing in Fig. 9 were all moving to the direction of low temperature during the reduction process compared with the peak of pure CeO₂. The layered structure on the surface of the HEOs benefited to the activation of various oxygen species and provided high performance.

2.2 Catalytic Performance

The catalytic performance of porous layered HEOs in the direct synthesis of DMC from CH₃OH and CO₂ was investigated, and the results were shown in Fig. 10. The yield of DMC was 7.2 mmol/g when 0.05 g HEO-1000 catalyst was used at 140 °C and 8 MPa (reaction pressure). The yield of DMC was 7.3 mmol/g when CeO₂ as catalyst under the same reaction conditions [29]. When HEO-1000 was used for the synthesis of DMC from CH₃OH and CO₂, the conversion of DMC increased exponentially with time. It took only 2–3 h for HEO-1000 to reach equilibrium at 140 °C and 8 MPa (reaction pressure), while it took about 5 h for CeO₂ to reach equilibrium under the same reaction conditions. The large pores, higher specific surface area, and the gap between the layers of HEO-1000 exposed more active sites, which ensured that CO₂ was sufficiently adsorbed by the catalyst, thus the catalytic efficiency of the catalyst was improved greatly. The HEO-1000 lattice was composed of five metal elements, and the differences in atomic radii and bond lengths can lead to severe distortion of the internal lattice of the solid solution [54, 55], which was called lattice distortion, as shown in Fig. 11. That is, enhancing S_{config} (configuration entropy), the binding of different types of cations in the same lattice was realized and enriched the number of oxygen vacancies in the active catalytic center. In addition, lattice distortion could also reduce the energy of the whole HEO system and promote and electron transfer of active species [56, 57].

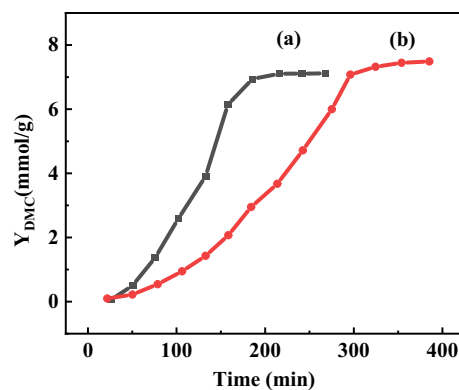


Fig. 10 Effect of reaction time on the yield of DMC over different catalysts: (a) HEO-1000, (b) CeO₂, Reaction conditions: 0.05 g catalyst, 15 mL CH₃OH, 140 °C, 8 MPa (reaction pressure)

2.3 Influence of Element Composition on Structure and Catalytic Performance of HEO

CH₃OH was dissociated into CH₃O⁻ and H⁺ on the catalyst [58, 59], while CO₂ was activated on the surface of the catalyst to produce a bidentate adsorption state and combined with CH₃O⁻ to form the methyl carbonate active intermediate [60, 61], and the catalyst could be considered as an ‘electron transfer station’.

Ce was in +4 valence states in the prepared HEOs, while La, Pr, Sm and Y were in +3 valence states. When the low-valence cations La, Pr, Sm and Y entered the high-valence cation Ce lattice to produce a covalent trend with the Ce⁴⁺ [62], due to the lack of an electron at this time, in order to maintain the electrical neutrality of the solid solution as a whole, a positively charged oxygen vacancy was formed by the lattice oxygen flowing to enhance the electron transfer capability [63], and the positively charged oxygen vacancies could play a role in transferring electrons from CH₃OH to CO₂ [60, 64]. The higher the content of positively charged oxygen vacancies in the catalyst, the stronger the ability of the catalyst to transfer electrons. Therefore, the content of

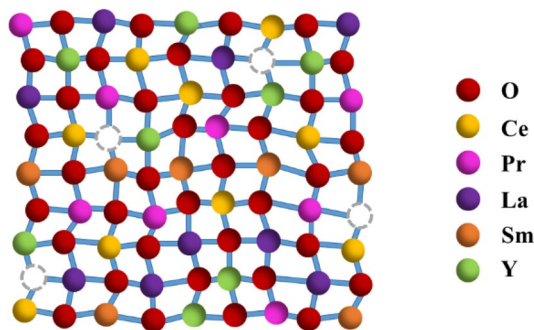


Fig. 11 Schematic diagram of lattice distortion of HEOs

tetravalent cerium in HEO were increased to form more positively charged oxygen vacancies on the catalyst surface, the conductivity of the catalyst and the electron transfer efficiency of CH_3OH and the catalyst surface were improved. In the direct synthesis of DMC from CO_2 and CH_3OH , the rate of CH_3OH dissociation and adsorption was much slower than that of CO_2 . In terms of kinetics, the process of CH_3OH giving electrons was the rate-controlling step of the reaction [65]. To improve the activation ability of CH_3OH was more favorable to improve the overall reaction activity.

It is not necessary for a solid-solution single phase of a HEOs to have an equimolar ratio distribution. Since the configurational entropy S_{config} is proportional to the logarithm of the number of element species of HEOs. The entropy was increased more slowly, when the number of elemental species is higher. That is, when the element species is more than 5, it is possible to form a solid solution single-phase structure even if the HEOs element composition is not equimolar [33, 66]. Therefore, the influence of high valence cation Ce^{4+} content on the catalytic performance was studied by no changing others rare earth elements, and it was expected that the ability of catalysts to transfer electrons could be improved by exploiting the conductivity of high entropy materials. $\text{Ce}_{0.5}(\text{LaPrSmY})_{0.5}\text{O}_{2-y}$ and $\text{Ce}_{0.8}(\text{LaPrSmY})_{0.2}\text{O}_{2-y}$ were obtained by increasing the content of Ce^{4+} in HEO-1000 to 50% and 80% while keeping the other four low-valent cations in the same molar ratio.

The XRD patterns of HEOs with different Ce^{4+} contents were shown in Fig. 12. It is shown that $\text{Ce}_{0.5}(\text{LaPrSmY})_{0.5}\text{O}_{2-y}$ still maintained the cubic fluorite structure. However, when the content of Ce element was increased to 80%, $\text{Ce}_{0.8}(\text{LaPrSmY})_{0.2}\text{O}_{2-y}$ appeared miscellaneous peaks at around 40° and $60\text{--}90^\circ$. The Jade crystal plane analysis showed that the second phase appeared in the solid solution, indicating that the Ce^{4+} content was

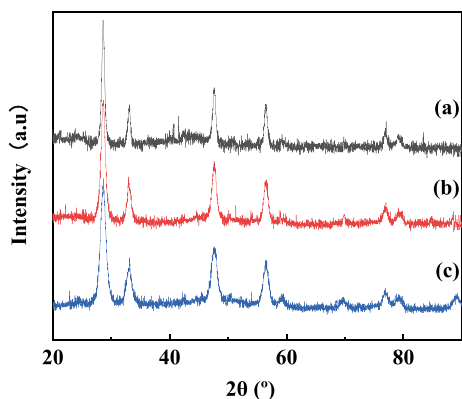


Fig. 12 XRD patterns of holey HEOs at varying Ce contents: (a) $\text{Ce}_{0.8}(\text{LaPrSmY})_{0.2}\text{O}_{2-y}$, (b) $\text{Ce}_{0.5}(\text{LaPrSmY})_{0.5}\text{O}_{2-y}$, (c) $\text{Ce}_{0.2}(\text{LaPrSmY})_{0.8}\text{O}_{2-y}$

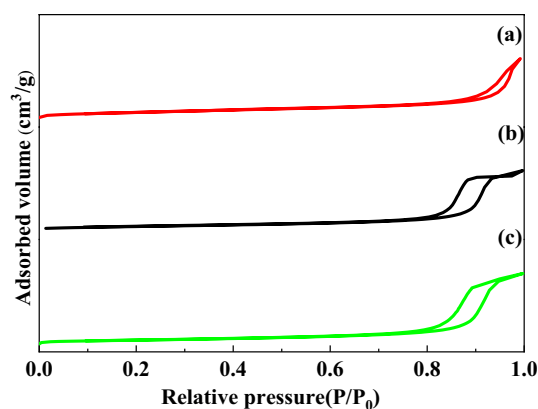


Fig. 13 N_2 adsorption–desorption isotherms of holey HEOs at different Ce contents: (a) $\text{Ce}_{0.8}(\text{LaPrSmY})_{0.2}\text{O}_{2-y}$, (b) $\text{Ce}_{0.5}(\text{LaPrSmY})_{0.5}\text{O}_{2-y}$, (c) $\text{Ce}_{0.2}(\text{LaPrSmY})_{0.8}\text{O}_{2-y}$

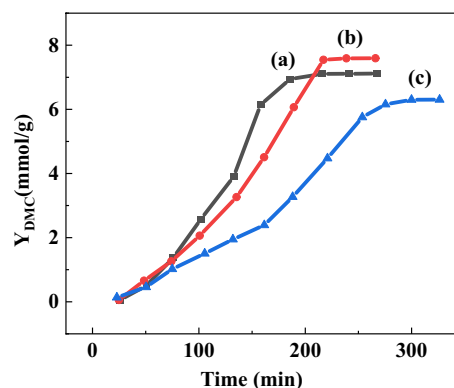


Fig. 14 Effect of reaction time on the yield of DMC: (a) $\text{Ce}_{0.2}(\text{LaPrSmY})_{0.8}\text{O}_{2-y}$, (b) $\text{Ce}_{0.5}(\text{LaPrSmY})_{0.5}\text{O}_{2-y}$, (c) $\text{Ce}_{0.8}(\text{LaPrSmY})_{0.2}\text{O}_{2-y}$ Reaction conditions: 0.05 g catalyst, 15 mL CH_3OH , 140°C , 8 MPa (reaction pressure)

excessive. HEOs lost a single fluorite structure because the lattice was destroyed to form a second phase.

The N_2 adsorption–desorption isotherms of pore-shaped HEOs at different Ce contents, and the results were shown in Fig. 13. BET analysis showed that the adsorption isotherms of $\text{Ce}_{0.5}(\text{LaPrSmY})_{0.5}\text{O}_{2-y}$ and $\text{Ce}_{0.8}(\text{LaPrSmY})_{0.2}\text{O}_{2-y}$ still exhibited the type IV adsorption isotherm. However, the hysteresis loop in the N_2 desorption curve of $\text{Ce}_{0.8}(\text{LaPrSmY})_{0.2}\text{O}_{2-y}$ was greatly attenuated when P/P_0 was 0.8. It is presumed that the mesoporous structure of the catalyst was covered by the collapse of the layered structure (Fig. 13). At this point, the specific surface area of the catalyst decreased from $100\text{ m}^2/\text{g}$ to $64\text{ m}^2/\text{g}$, then the collision probability of CH_3OH and CO_2 on the catalyst surface decreased, and the activity of the catalyst decreased.

HEOs with different Ce content was used for synthesis of DMC from CH_3OH and CO_2 , and the results were shown

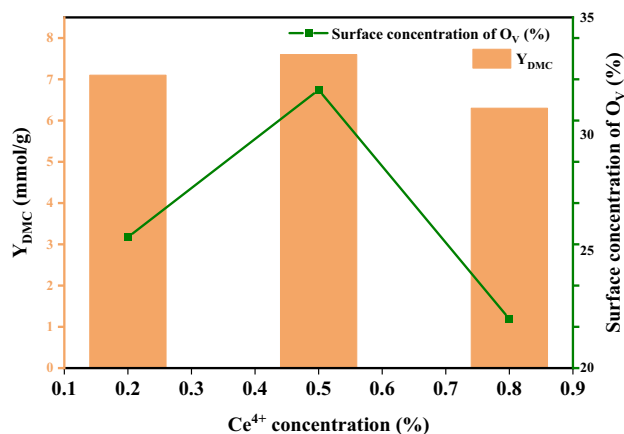


Fig. 15 Effect of surface oxygen vacancy content of HEOs with different Ce content on the yield of DMC, Reaction conditions: 0.05 g catalyst, 15 mL CH₃OH, 140 °C, 8 MPa (reaction pressure)

in Fig. 14. The results of the catalytic activity test showed that when Ce⁴⁺ content was increased from 20 to 50%, the DMC yield increased from 7.1 mmol/g to 7.6 mmol/g when the reaction time is 200 min. When the Ce content was further increased to 80%, the DMC yield and conversion rate decreased significantly, and the DMC yield decreased to 6 mmol/g.

As the Ce⁴⁺ content increased from 20 to 80%, the oxygen vacancy content of the HEOs surface and the yield of DMC in the activity test changed, the results were shown in Fig. 15. With the increased of Ce⁴⁺ content from 20 to 50%, the oxygen vacancy content on the catalyst surface increased from 25.6% to 31.9%. However, when Ce⁴⁺ content increased from 50 to 80%, the oxygen vacancy concentration decreased to 22%. It could be seen that the oxygen vacancy concentration was positively correlated with the catalytic performance of the HEOs. The adsorption and activation of CH₃OH by some additional positively charged oxygen vacancies increased the ability to receive negatively charged methoxy, that is, the increased content of positively charged oxygen vacancies effectively enhanced the ability of the catalyst surface to transfer electrons. In addition, it could be seen from Fig. 15 that the Ce content has a significant influence on the yield of DMC which is due to the fact that the carbonylation process of DMC has a high spatial site resistance and the reduction in the content of oxygen vacancies in the catalyst reduced the adsorption capacity of CO₂ and CH₃OH molecules and hindered the formation of C-O bonds [67]. The proposed mechanism of DMC formation from CO₂ and CH₃OH at the surface oxygen vacancies over catalysts as shown in Fig. 16 [59].

The TEM images of Ce_{0.5}(LaPrSmY)_{0.5}O_{2-y} and Ce_{0.8}(LaPrSmY)_{0.2}O_{2-y} were shown in Fig. 17. The Ce_{0.8}(LaPrSmY)_{0.2}O_{2-y} cannot form a well-defined high-entropy structure because the Ce content was too high

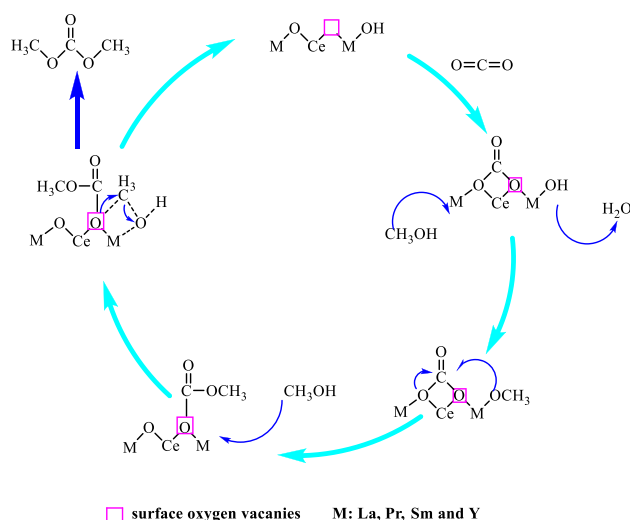


Fig. 16 Proposed mechanism of DMC formation from CO₂ and CH₃OH at the surface oxygen vacancies over catalysts

to maintain the high dispersion of each atom on the molecular level. The shaded part of the picture might be a large agglomeration of Ce atoms. Combined with the BET results in Fig. 13, it could be seen that the pore of Ce_{0.8}(LaPrSmY)_{0.2}O_{2-y} was blocked, the lamellar structure was collapsed, and the specific surface area was decreased. The collapse of the structure and atomic aggregation lead to the coverage of oxygen vacancies on the catalyst surface, resulting in the inability of CH₃OH and CO₂ to be fully adsorbed by the catalyst, which reduced the catalyst activity. Combined with the XRD patterns of Fig. 12, it could be seen that Ce_{0.8}(LaPrSmY)_{0.2}O_{2-y} appeared a second phase at this time, resulting in lattice rupture. The conductivity of the catalyst was proportional to the hole concentration and hole mobility. The disruption of the lattice will reduce the rate of electron migration, which will affect the rate of electron transfer on the catalyst surface.

In summary, the content of positively charged oxygen vacancies on the catalyst surface could be increased by

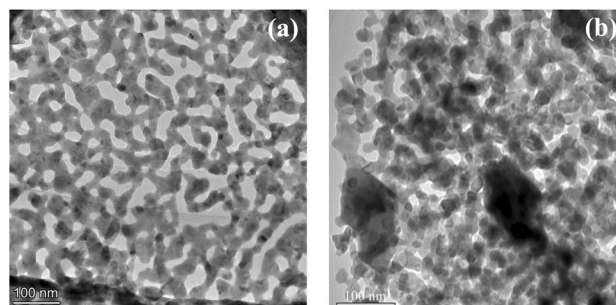


Fig. 17 TEM images of holey HEOs at different Ce contents: (a) Ce 50%, (b) Ce 80%

changing the content of high-valent cations in HEOs, and the catalytic performance of HEOs were improved. And excessive content of a single element will prevent various atoms from dispersing on the molecular level, the porous layered structure in HEOs will be destroyed, and the S_{config} of HEOs are reduced, then HEOs cannot maintain a single cubic fluorite structure. The specific surface area and oxygen vacancy content of HEOs in the disrupted single crystalline phase were reduced, resulting in lower catalyst performance as well as electron transfer efficiency.

3 Conclusions

$\text{Ce}_x(\text{LaPrSmY})_{1-x}\text{O}_{2-y}$ porous fluorite HEOs catalysts were synthesized by anchoring method. DMC was synthesized from CH_3OH and CO_2 by using $\text{Ce}_{0.5}(\text{LaPrSmY})_{0.5}\text{O}_{2-y}$ as a catalyst, and the yield of DMC was as high as 7.6 mmol/g at 140 °C and 8.0 MPa (reaction pressure). Under the same conditions, $\text{Ce}_{0.5}(\text{LaPrSmY})_{0.5}\text{O}_{2-y}$ reached the reaction equilibrium was in half the time of CeO_2 . The reaction rate for the direct synthesis of DMC from CH_3OH and CO_2 on $\text{Ce}_{0.5}(\text{LaPrSmY})_{0.5}\text{O}_{2-y}$ was enhanced, attributed to the abundant oxygen vacancies on the surface and the excellent electron transfer ability. When the content of valent cation Ce^{4+} in HEOs increased from 20 to 50%, the catalytic performance was improved due to lattice distortion and more oxygen vacancies. When the content of Ce^{4+} increased to 80%, the fluorite crystal in HEOs were destroyed, a second crystal phase was produced, and the catalytic performance decreased.

Supplementary Information The online version contains supplementary material available at <https://doi.org/10.1007/s10562-023-04303-4>.

Authors contribution All authors have made substantial contributions to the work reported. YG: Investigation, Data curation, Writing—Original Draft. XL: Methodology, Visualization. SZ: Formal analysis, Investigation. ZW: Formal analysis, Investigation. QC: Conceptualization, Writing—Review and Editing, Funding acquisition. YW: Methodology, supervision.

Data Availability The data presented in this study are available in supplementary material. Sample Availability Samples of all the compounds are available from the authors.

Declarations

Conflict of Interest The authors declare that they have no known competing financial interests or personal relationships that could have appeared to influence the work reported in this paper.

References

- Sarkar A, Wang Q, Schiele A, Chellali MR, Bhattacharya SS, Wang D, Brezesinski T, Hahn H, Velasco L, Breitung B (2019) *Adv Mater* 31:1806236
- Sarkar A, Djenadic R, Usharani NJ, Sanghvi KP, Chakravadhanula VSK, Gandhi AS, Hahn H, Bhattacharya SS (2017) *J Eur Ceram Soc* 37:747
- San S, Ching WY (2020) *Front Mater* 7:575262
- Chen H, Fu J, Zhang P, Peng H, Abney CW, Jie K, Liu X, Chi M, Dai S (2018) *J Mater Chem A* 6:11129
- Wright AJ, Huang C, Walock MJ, Ghoshal A, Murugan M, Luo J (2020) *J Am Ceram Soc* 104:448
- Gild J, Samiee M, Braun JL, Harrington T, Vega H, Hopkins PE, Vecchio K, Luo J (2018) *J Eur Ceram Soc* 38:3578
- Salian A, Mandal S (2021) *Crit Rev Solid State Mater Sci* 47:142
- Sarkar A, Kruk R, Hahn H (2021) *Dalton Trans* 50:1973
- Chen K, Ma J, Tan C, Li C, An L (2021) *Ceram Int* 47:21207
- Lyu WY, Liu WD, Li M, Hong M, Guo K, Luo J, Xing J, Sun Q, Xu S, Zou J, Chen ZG (2022) *Chem Eng J* 446:137278
- Lastovina TA, Bugaev AL, Kubrin SP, Kudryavtsev EA, Soldatov AV (2017) *J Struct Chem* 57:1444
- Yan JQ, Li P, Ji YJ, Bian H, Li YY, Liu SZ (2017) *J Mater Chem A* 5:21478
- Pereira HA, Mironuk FL, Menezes BBD, Duarte R, Villetti MA, Hilgemann M, Rosa MBD (2019) *Thermochim Acta* 678:178315
- Hume RW, Powell HM (1935) *Z Krist* 91:23
- Goldschmidt VM (1926) *Naturwissenschaften* 14:477
- Ushakov SV, Hayun S, Gong W, Navrotsky A (2020) *Materials (Basel)* 13:3141
- Selva M, Perosa A, Rodríguez PD, Luque R (2019) *ACS Sustain Chem Eng* 7:6471
- Pyo SH, Park JH, Chang TS, Hatti KR (2017) *Curr Opin Green Sustain Chem* 5:61
- Daniele D, Franco R, Ugo R (2001) *Applied Catalysis A* 221:241
- Tan HZ, Wang ZQ, Xu ZN, Sun J, Xu YP, Chen QS, Chen Y, Guo GC (2018) *Catal Today* 316:2
- Kohli K, Sharma BK, Panchal CB (2022) *Energies* 15:5133
- Zheng HY, Wang JZ, Li Z, Yan LF, Wen JZ (2016) *Fuel Process Technol* 152:367
- Liu M, Konstantinova M, Negahdar L, McGregor J (2021) *Chem Eng Sci* 231:116267
- Mandoie M, Rahimi M, Nikravesh G, Salehi E (2022) *J Indus Eng Chem*
- Peng B, Dou H, Shi H, Ember EE, Lercher JA (2018) *Catal Lett* 148:1914
- Liu K, Liu C (2021) *RSC Adv* 11:35711
- Sun W, Zheng L, Wang Y, Jia W, Guo W, Liu Z, Ding X, Wu L, Fang T (2022) *J CO2 Util* 58:101912
- Giram GG, Bokade VV, Srinivas D (2018) *New J Chem* 42:17546
- Wang S, Zhao L, Wang W, Zhao Y, Zhang G, Ma X, Gong J (2013) *Nanoscale* 5:5582
- Liu H, Zhu D, Jia B, Huang Y, Cheng Y, Luo X, Liang Z (2022) *Chem Eng Sci* 254:117614
- Sun YG, Xia YN (2002) *Science* 298:2176
- Faria DJ, Santos LMD, Bernard FL, Pinto IS, Resende MAC, Einloft S (2020) *RSC Adv* 10:34895
- Sarkar A, Breitung B, Hahn H (2020) *Scripta Mater* 187:43
- Gao M, Lu M, Zhang X, Luo Z, Xiao J (2022) *Polymers (Basel)* 14:2419
- Hao PP, Xie MJ, Chen SY, Li MH, Bi FF, Zhang Y, Lin M, Guo XK, Ding WP, Guo XF (2020) *Sci Adv* 6:7031
- Ketola AE, Leppanen M, Turpeinen T, Papponen P, Strand A, Sundberg A, Arstila K, Retulainen E (2019) *RSC Adv* 9:15668

37. Li Z, Wang D, Shen J, Chen J, Wu C, Qu Z, Luo K, Meng Z, Li Y (2021) *Materials* (Basel) 14:5465
38. Yu G, Chen W, Zhao J, Nie Q (2006) *J Appl Electrochem* 36:1021
39. Neumann S, Grotheer S, Tielke J, Schrader I, Quinson J, Zana A, Oezaslan M, Arenz M, Kunz S (2017) *J Mater Chem A* 5:6140
40. Thirumalairajan S, Girija K (2020) *Nanoscale Adv* 2:3570
41. Fracchia M, Ghigna P, Pozzi T, Anselmi TU, Colombo V, Braglia L, Torelli P (2020) *J Phys Chem Lett* 11:3589
42. Johnstone GHJ, Gonzalez RMU, Taddei KM, Sutarto R, Sawatzky GA, Green RJ, Oudah M, Hallas AM (2022) *J Am Chem Soc* 144:20590
43. Wang J, Luo L, Han C, Yun R, Tang X, Zhu Y, Nie Z, Zhao W, Feng Z (2019) *Materials* (Basel) 12:1444
44. Qi H, Jiantao N, KeQin Z, Mu Y (2022) *Materials* 15:4723
45. Zhang B, Zhang S, Liu B (2020) *Appl Surf Sci* 529:147068
46. Devaiah D, Tsuzuki T, Aniz CU, Reddy BM (2015) *Catal Lett* 145:1206
47. Dąbrowa J, Szymczak M, Zajusz M, Miśka A, Moździerz M, Berent K, Wyrwał SM, Bernasik A, Stygar M, Świerczek K (2020) *J Eur Ceram Soc* 40:5870
48. Sharma JK, Srivastava P, Ameen S, Akhtar MS, Sengupta SK, Singh G (2017) *Mater Res Bull* 91:98
49. Natile MM, Galenda A, Glisenti A (2008) *Surf Sci Spectra* 15:1
50. Nallabala NKR, Godavarthi S, Kummara VK, Kesarla MK, Yuvaraj C, Suresh K, Ravi N, Guntupalli GK, Jilani SAK, Vattikuti SVP (2021) *Sol Energy Mater Sol Cells* 225:111033
51. Yin LX, Zhang DD, Wang D, Wang FF, Huang JF, Kong XG, Zhang H, Liu CQ (2016) *Ceram Int* 42:11998
52. Lee ML, Kao CH, Chen H, Lin CY, Chung YT, Chang KM (2017) *Ceram Int* 43:3043
53. Jiang Y, Wang X, Bao C, Huang S, Zhang X, Wang X (2017) *Korean J Chem Eng* 34:1874
54. Usharani NJ, Bhandarkar A, Subramanian S, Bhattacharya SS (2020) *Materialia* 200:526
55. Abhishek S, Leonardo V, Wang D, Wang QS, Gopichand T, Lead B, Christian K, Torsten B, Horst H, Ben B (2018) *Nate Commun* 9:3400
56. Owen LR, Jones NG (2018) *J Mater Res* 33:2954
57. Clausen CM, Pedersen JK, Batchelor TAA, Rossmeisl J (2021) *Nano Res* 15:4775
58. Wang HF, Gong XQ, Guo YL (2009) *J Phys Chem C Nanomater Interfaces* 113:10229
59. Liu B, Li C, Zhang GQ, Yao XS, Chuang SSC, Li Z (2018) *ACS Catal* 8:10446
60. Chen S, Wang H, Kang Z, Jin S, Zhang X, Zheng X, Qi Z, Zhu J, Pan B, Xie Y (2019) *Nat Commun* 10:788
61. Xie S, Bell AT (2000) *Catal Lett* 70:137
62. Jung J, Atanasov M, Neese F (2017) *Inorg Chem* 56:8802
63. Sohn H, Celik G, Gunduz S, Dogu D, Zhang S, Shan J, Tao FF, Ozkan US (2017) *Catal Lett* 147:2863
64. Zhao Z, Xiang H, Dai F-Z, Peng Z (2019) *Zhou Y* 35:2647
65. Zhao SY, Wang SP, Zhao YJ, Ma XB (2017) *Chin Chem Lett* 28:65
66. R. J P, WLNC L, Bo J, Sreya P, Daniel O, A. G D, Katharine P (2021) 18:2101323.
67. Ji S, Chen Y, Zhao G, Wang Y, Sun W, Zhang Z, Lu Y, Wang D (2022) *Appl Catal B* 304:120922

Publisher's Note Springer Nature remains neutral with regard to jurisdictional claims in published maps and institutional affiliations.

Springer Nature or its licensor (e.g. a society or other partner) holds exclusive rights to this article under a publishing agreement with the author(s) or other rightsholder(s); author self-archiving of the accepted manuscript version of this article is solely governed by the terms of such publishing agreement and applicable law.

Authors and Affiliations

Yunhan Gu¹ · Qingyan Cheng^{1,2} · Xu Li¹ · Shuai Zhang¹ · Zhuo Wang¹ · Yanji Wang^{1,2}

✉ Qingyan Cheng
chengqingyan@hebut.edu.cn

² Tianjin Key Laboratory of Chemical Process Safety,
Tianjin 300401, China

¹ School of Chemical Engineering and Technology, Hebei
University of Technology, Tianjin 300401, China